Chapter 2
First-Order Time-Delayed Chaotic Systems: Design and Experiment

In this chapter, we discuss the design principle of chaotic time-delayed systems with (i) a bimodal nonlinearity and (ii) an unimodal nonlinearity. Both the nonlinearities are represented by *closed-form mathematical functions* (unlike PWL nonlinearity). We carry out rigorous stability analysis to identify the Hopf bifurcation through which limit cycle oscillations are born. Next, we simulate the system models numerically to show that with the variation of delay and other system parameters, the systems show chaos. Complexity of the systems is characterized by Lyapunov exponents and Kaplan–Yorke dimension. Finally, we discuss in detail how both the systems can be implemented in experiment using electronic circuits.

2.1 Chaotic Time-Delayed System with Bimodal Nonlinearity: System Description

We consider the following first-order nonlinear retarded-type delay differential equation with a single constant scalar delay

$$\dot{x}(t) = -ax(t) + bf(x_\tau), \tag{2.1}$$

where $a > 0$ and b are system parameters. Also, $x_\tau \equiv x(t-\tau)$, where $\tau \in \mathscr{R}^+$ is a constant time delay. Now, we define the following closed-form mathematical function for the nonlinearity:

$$f(x_\tau) = -nx_\tau + m\tanh(lx_\tau), \tag{2.2}$$

where n, m, and l are all positive system parameters and they are restricted by the following constraint $n < ml$ to maintain the bimodal nature of the nonlinearity. It can be seen that the nonlinear function is constituted by the weighted superposition

D. Biswas and T. Banerjee, *Time-Delayed Chaotic Dynamical Systems*, SpringerBriefs in Nonlinear Circuits,
https://doi.org/10.1007/978-3-319-70993-2_2

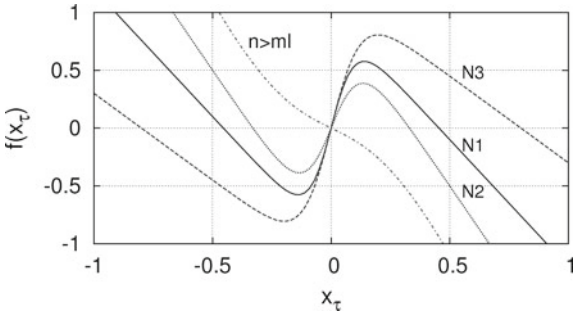

Fig. 2.1 Nonlinearity with the function $f(x_\tau) = -nx_\tau + m\tanh(lx_\tau)$ with "N1": $n = 2.2$, $m = 1$, $l = 10$; "N2": $n = 3$, $m = 1$, $l = 8$, "N3": $n = 1.5$, $m = 1.2$, $l = 8$. Dashed curve is for $n = 4$, $m = 1$, $l = 3$, which shows that for $n > ml$ the nonlinearity does not show the bimodal nature

of two functions, namely the linear proportionality function and the nonlinear $\tanh(\cdot)$ function. Further, $f(x_\tau)$ is an odd-symmetric function, i.e., $f(-x_\tau) = -f(x_\tau)$.

Figure 2.1 shows the nature of the nonlinearity produced by $f(x_\tau)$ for different values of n, m, and l. The nonlinearity shows a hump in the first and the third quadrants. The condition $n < ml$ ensures this bimodal nature of the nonlinear function. Tamaševičius et al. [135] used almost similar form of the nonlinearity with piecewise linear (PWL) function; but unlike their system, here Eq. (2.2) has a closed-form mathematical function that does not show sharp corners in the turning points. The nonlinear functions of Fig. 2.1 shows that positive slope continuously changes to the negative slope through a zero slope region. The PWL function is unable to represent this behavior. Also, in the electronic circuit experiment, it is hard to realize a sharp transition from positive to negative slope due to the nonideal characteristics of the practical circuit components (see e.g., [135]). Therefore, the closed-form mathematical model of the nonlinearity used here is suitable for the electronic circuit implementation. Also, Eq. (2.2) provides a large number of choices of n, m, and l for which the bimodal nature will be preserved. Further, Ref. [135] considered only positive values of b, but here we consider both positive and negative values of b.

2.2 Stability and Bifurcation Analysis

2.2.1 Positive b

The stability of the system is analyzed by rewriting Eq. (2.1) in the following form:

$$\dot{x} = g\big(x(t), x_\tau\big) = -ax(t) + bf(x_\tau). \tag{2.3}$$

The equilibrium condition implies $\dot{x} = 0$ and $x(t) = x_\tau = x^*$ (say), i.e., $g(x^*, x^*) = -ax^* + bf(x^*) = 0$, which gives

$$\tanh(lx^*) = \frac{a + nb}{mb}x^*. \tag{2.4}$$

Close inspection reveals that Eq. (2.4) has a fixed point $x^* = 0$ for $l \leq \frac{a+nb}{mb}$, i.e., we have a single trivial fixed point at $x^* = 0$ for

$$b \leq \frac{a}{-n + ml}. \tag{2.5}$$

For $b > \frac{a}{-n+ml}$, Eq. (2.4) has three fixed points, namely $x^* = (-p1, 0, p1)$. Here, $\pm p1$ are the nontrivial fixed points whose values are determined by the system parameters.

Let us now examine the stability of each fixed point. From Eq. (2.3), one gets

$$J_0 = \frac{\partial g(x, x_\tau)}{\partial x} = -a, \tag{2.6}$$

and

$$J_\tau\big|_{x_\tau = x^*} = \frac{\partial g(x, x_\tau)}{\partial x_\tau}\bigg|_{x_\tau = x^*} = b\big[-n + ml\ \mathrm{sech}^2(lx^*)\big]. \tag{2.7}$$

The *characteristic equation* of the system is given by $J_0 + J_\tau e^{-\lambda\tau} - \lambda = 0$, which gives

$$\lambda = -a + b\big[-n + ml\ \mathrm{sech}^2(lx^*)\big]e^{-\lambda\tau}. \tag{2.8}$$

Stability for $\tau = 0$
For the case of $\tau = 0$, the characteristic equation takes the following form:

$$\lambda = J_0 + J_\tau. \tag{2.9}$$

Taking $\lambda = \mu + i\nu$, and comparing real and imaginary parts in both sides of the above equation, one gets

$$\mu = -a + b\big[-n + ml\ \mathrm{sech}^2(lx^*)\big], \quad \text{and} \quad \nu = 0. \tag{2.10}$$

Asymptotic stability will occur when all the roots of the characteristic equation have negative real parts (i.e., negative μ); from Eq. (2.10), we get the condition of stability as

$$b\big[-n + ml\ \mathrm{sech}^2(lx^*)\big] < a. \tag{2.11}$$

Equation (2.11) imposes the first condition for choosing the system parameters to achieve asymptotic stability of the system for $\tau = 0$. Let us now examine the case for $x^* = 0$; from Eq. (2.11), we have the condition for stability as $b < -n+ml$, which is interestingly identical with Eq. (2.5). Thus, one can conclude that, for $b < -n+ml$, $x^* = 0$ is the only stable fixed point for any $\tau \geq 0$, but beyond that, $x^* = 0$ becomes unstable through a *supercritical pitchfork bifurcation* and two nontrivial fixed points ($\pm p1$) emerge. Next, we have to examine the stability of the nontrivial fixed points ($\pm p1$).

Stability for $\tau \neq 0$

Hopf bifurcation will appear if at least one of the eigenvalues crosses the imaginary axis from left, and enter the right half plane. Thus, if μ varies from left to right, we can say that $\mu < 0$ represents a stable state, $\mu > 0$ is bifurcated state, and $\mu = 0$ is the bifurcation point. At the emergence of Hopf bifurcation, we assume $\mu = 0$; thus using $\lambda = i\nu$, we get

$$\begin{aligned} J_0 + J_\tau e^{-i\nu\tau} - i\nu = 0, \\ J_0 + J_\tau \cos(\nu\tau) - i\{J_\tau \sin(\nu\tau) + \nu\} = 0. \end{aligned} \tag{2.12}$$

Now equating the real and imaginary parts on both sides of the above equation, we get

$$J_\tau \cos(\nu\tau) = -J_0, \tag{2.13}$$

$$J_\tau \sin(\nu\tau) = -\nu. \tag{2.14}$$

Equations (2.13) and (2.14) lead to give $\nu = \sqrt{J_\tau^2 - J_0^2}$. This is possible only for $|J_\tau| \geq |J_0|$, i.e.,

$$\left|b[-n + ml\ \mathrm{sech}^2(lx^*)]\right| \geq \left|-a\right|. \tag{2.15}$$

Again from Eq. (2.13), we get

$$\nu\tau = \cos^{-1}\left(-\frac{J_0}{J_\tau}\right), \tag{2.16}$$

which leads to

$$\tau_{k1} = \frac{\left[\cos^{-1}\left(-\frac{J_0}{J_\tau}\right) + 2k\pi\right]}{\sqrt{{J_\tau}^2 - {J_0}^2}}, \quad \text{for } J_\tau < 0, \tag{2.17a}$$

$$\tau_{k2} = \frac{\left[\left\{2\pi - \cos^{-1}\left(-\frac{J_0}{J_\tau}\right)\right\} + 2k\pi\right]}{\sqrt{{J_\tau}^2 - {J_0}^2}}, \quad \text{for } J_\tau > 0, \tag{2.17b}$$

where $k = 0, 1, 2, \ldots$ Now we set $\nu_0 = \sqrt{{J_\tau}^2 - {J_0}^2}$. Let $\lambda_k(\tau) = \mu_k(\tau) + i\nu_k(\tau)$ be a root of Eq. (2.1) near $\tau = \tau_k$ satisfying $\mu_k(\tau_k) = 0$ and $\nu_k(\tau_k) = \nu_0$. We have

$$\lambda = J_0 + J_\tau e^{-\lambda\tau}, \tag{2.18a}$$

$$\lambda = -a + b[-n + ml\ \mathrm{sech}^2(lx^*)]e^{-\lambda\tau}. \tag{2.18b}$$

We put

$$s = b[-n + ml\ \mathrm{sech}^2(lx^*)]. \tag{2.19}$$

Differentiating both sides of Eq. (2.18b) with respect to τ, we get

$$\begin{aligned} \frac{d\lambda}{d\tau} &= se^{-\lambda\tau}\left(-\lambda - \tau\frac{d\lambda}{d\tau}\right), \\ \frac{d\lambda}{d\tau} &= \frac{-\lambda s e^{-\lambda\tau}}{1 + \tau s e^{-\lambda\tau}}. \end{aligned} \tag{2.20}$$

Again, from equation Eq. (2.19), we have $se^{-\lambda\tau} = \lambda + a$, we put this in the above and get

$$\frac{d\lambda}{d\tau} = \frac{-\lambda(\lambda + a)}{1 + \tau(\lambda + a)}.$$

Now, at $\tau = \tau_k$; $\lambda = i\nu_0$, as $\mu_k(\tau_k) = 0$ there, hence,

$$\left.\frac{d\lambda}{d\tau}\right|_{\tau=\tau_k} = \frac{{\nu_0}^2 - i\nu_0 a}{(1 + \tau a) + i\tau\nu_0}. \tag{2.21}$$

Equating the real parts on both sides, we get

$$\mu'(\tau_k) = \frac{{\nu_0}^2}{(1 + \tau a)^2 + \tau^2\nu_0^2}.$$

Thus,

$$\mu'(\tau_k) > 0. \tag{2.22}$$

For all values of above-mentioned x^*, Eq. (2.22) is valid. So we conclude that the stable state lies between $\tau = 0$ and τ_{01}.

Now, let us investigate the stability of the system for the following parameter set: $a = 1$, $n = 2.2$, $m = 1$, and $l = 10$ (as we have used in "N1" of Fig. 2.1). Figure 2.2 shows the first six stability curves τ_{ki} $(i = 1, 2)$ (Using Eq. (2.17)) in the $b - \tau$ parameter space. In the figure, τ_{k1} and τ_{k2} are represented by solid lines and dotted lines, respectively. Since $\mu'(\tau_k) > 0$ for any $k = 0, 1, 2\ldots$, thus, stability zone cannot be situated between two consecutive τ_{ki} curves. So we conclude that the stable island lies between $\tau = 0$ and τ_{01} curves. The shaded region in the figure represents the stable zone, and τ_{01} curve represents the Hopf bifurcation curve. Let us now summarize the stability scenario of the system for $b \geq 0$: (i) $x^* = 0$: for this fixed point, the condition of stability reads $b < \frac{1}{-n+ml}$ for any $\tau \geq 0$. Beyond this value of b, for any $\tau \geq 0$, the trivial fixed point $x^* = 0$ becomes unstable through a pitchfork bifurcation and $\pm p1$ fixed points emerge. (ii) $x^* = \pm p1$: These two nontrivial fixed points come into play for $b \geq \frac{1}{-n+ml}$. Since at these fixed points $|J_\tau| > |-a|$, thus

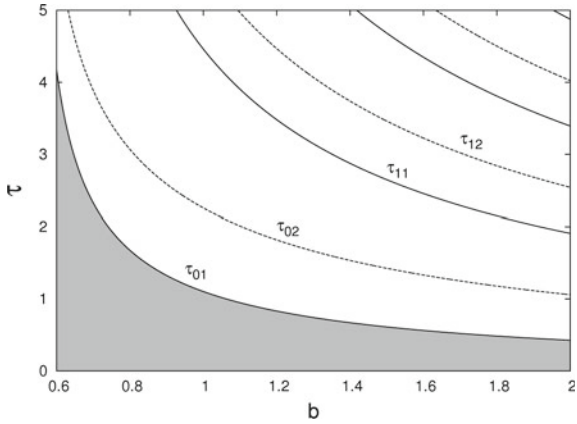

Fig. 2.2 Stability zone in the b–τ ($b > 0$) parameter space with parameters $a = 1$, $n = 2.2$, $m = 1$, and $l = 10$. Shaded region indicates the zone of stable fixed point

the system depicts a stable fixed point for the delay τ, in $0 \leq \tau < \tau_{01}$. Beyond $\tau = \tau_{01}$, Hopf bifurcation occurs and a stable limit cycle appears.

Next, we study the direction of Hopf bifurcation and the stability of the bifurcating solutions for $x^* = \pm p1$ at $\tau = \tau_{01}$. Using the techniques described by Wei [144], let us define

$$D = \frac{1}{1 + \tau_{01} a - i\tau_{01}\nu_0}. \tag{2.23}$$

We can obtain the following coefficients:

$$\begin{aligned}
g_{20} &= \bar{D} b \tau_{01} f''(x^*) e^{-2i\tau_{01}\nu_0}, \\
&= -2\bar{D} b \tau_{01} m l^2 \operatorname{sech}^2(lx^*) \tanh(lx^*) e^{-2i\tau_{01}\nu_0}, \\
g_{11} &= \bar{D} b \tau_{01} f''(x^*), \\
&= -2\bar{D} b \tau_{01} m l^2 \operatorname{sech}^2(lx^*) \tanh(lx^*), \\
g_{02} &= \bar{D} b \tau_{01} f''(x^*) e^{2i\tau_{01}\nu_0}, \\
&= -2\bar{D} b \tau_{01} m l^2 \operatorname{sech}^2(lx^*) \tanh(lx^*) e^{2i\tau_{01}\nu_0},
\end{aligned} \tag{2.24}$$

$$\begin{aligned}
g_{21} &= \bar{D} b \tau_{01} \Big[f''(x^*) \{ e^{-i\tau_{01}\nu_0} W_{11}(-1) + e^{i\tau_{01}\nu_0} W_{20}(-1) \} + f'''(x^*) e^{-i\tau_{01}\nu_0} \Big], \\
&= -2ml^2 \bar{D} b \tau_{01} \operatorname{sech}^2(lx^*) \Big[\{ e^{-i\tau_{01}\nu_0} W_{11}(-1) + e^{i\tau_{01}\nu_0} W_{20}(-1) \} \tanh(lx^*) \\
&\qquad - l\{2 - 3\operatorname{sech}^2(lx^*)\} e^{-i\tau_{01}\nu_0} \Big],
\end{aligned}$$

where

$$
\begin{aligned}
W_{20}(-1) &= -\frac{g_{20}}{i\tau_{01}\nu_0}e^{-i\tau_{01}\nu_0} - \frac{\bar{g}_{02}}{3i\tau_{01}\nu_0}e^{i\tau_{01}\nu_0} + E_1 e^{-2i\tau_{01}\nu_0},\\
W_{11}(-1) &= \frac{g_{11}}{i\tau_{01}\nu_0}e^{-i\tau_{01}\nu_0} - \frac{\bar{g}_{11}}{i\tau_{01}\nu_0}e^{i\tau_{01}\nu_0} + E_2,\\
E_1 &= \frac{bf''(x^*)e^{-2i\tau_{01}\nu_0}}{2i\nu_0 + a - bf'(x^*)e^{-2i\tau_{01}\nu_0}},\\
&= \frac{-b\{2ml^2\ \mathrm{sech}^2(lx^*)\tanh(lx^*)\}e^{-2i\tau_{01}\nu_0}}{2i\nu_0 + a - b\big[-n + ml\ \mathrm{sech}^2(lx^*)\big]e^{-2i\tau_{01}\nu_0}},
\end{aligned}
$$

and

$$
\begin{aligned}
E_2 &= \frac{bf''(x^*)}{a - bf'(x^*)},\\
&= \frac{-2bml^2\ \mathrm{sech}^2(lx^*)\tanh(lx^*)}{a - b\big[-n + ml\ \mathrm{sech}^2(lx^*)\big]}.
\end{aligned}
$$

Because each g_{ij} in equation set (2.24) is expressed by the parameters and delay, we can compute the following quantities:

$$
\begin{aligned}
c_1(0) &= \frac{i}{2\tau_{01}\nu_0}\left(g_{11}g_{20} - 2|g_{11}|^2 - \frac{|g_{02}|^2}{3}\right) + \frac{g_{21}}{2},\\
\mu_2 &= -\frac{\mathrm{Re}(c_1(0))}{\mathrm{Re}(\lambda'(\tau_{01}))},\\
\beta_2 &= 2\mathrm{Re}(c_1(0)),\\
T_2 &= -\frac{\mathrm{Im}(c_1(0)) + \mu_2\mathrm{Im}(\lambda'(\tau_{01}))}{\nu_0}.
\end{aligned}
\tag{2.25}
$$

The parameter μ_2 determines the direction of the Hopf bifurcation: if $\mu_2 > 0$ ($\mu_2 < 0$), then the Hopf bifurcation is *supercritical (subcritical)* and the bifurcating periodic solutions exist for $\tau > \tau_{01}$ ($\tau < \tau_{01}$). β_2 determines the stability of bifurcating periodic solutions: the bifurcating periodic solutions are orbitally asymptotically *stable (unstable)* if $\beta_2 < 0$ ($\beta_2 > 0$). Finally, T_2 determines the period of bifurcating periodic solutions: the period *increases (decreases)* if $T_2 > 0$ ($T_2 < 0$).

To test the validity of our analysis, let us use the following parameter values: $a = 1, n = 2.2, m = 1$, and $l = 10$. For $b = 1$, we have $p1 = 0.31$, $J_0 = -a = -1$, and $J_\tau = b[-n + ml\ \mathrm{sech}^2(\pm lp_1)] = -2.121$. Thus, we see that $|J_\tau| > |J_0|$ (satisfying Eq. (2.16)). Also, at these parameter values, we have $\tau_{01} = 1.102$ (from Eq. (2.17)). Thus, we expect that at $b = 1$ and $\tau_{01} = \tau_H = 1.102$, the fixed point losses its stability through Hopf bifurcation. Further, at these parameter values, we have $g_{11} = -0.421 + 0.413i$, $g_{20} = 0.582 + 0.095i$, $g_{02} = -0.11 - 0.58i$, $g_{21} = -11.622 - 3.812i$, $E_1 = -0.217 - 0.082i$, $E_2 = -0.525$, $W_{20} = 0.519 - 0.302i$,

$W_{11} = -0.354$, and $c_1(0) = -5.86 - 2.172i$. Using these set of values in Eq. (2.25), we have $\mu_2 = 14.524 > 0$; that means the resulting bifurcation is a *supercritical* Hopf bifurcation. Also, since $\beta_2 = -11.72 < 0$, thus the bifurcating periodic solutions are orbitally asymptotically stable. Finally, $T_2 = 11.142 > 0$ indicates that the period of the limit cycle increases with increasing τ.

2.2.2 *Negative* b

Let us define $b = -b_1$, where $b_1 > 0$. For negative b, we have

$$ax^* = -b_1 f(x^*). \tag{2.26}$$

This gives the following equation: $\tanh(lx^*) = -\frac{a-nb_1}{mb_1}x^*$. Again a close observation reveals that for $b_1 \leq \frac{a}{n}$, one has only one trivial fixed point, which is $x^* = 0$; beyond this value of b, there exists three equilibrium points, namely $x^* = q1,\ 0,$ and $-q1$. Using the similar arguments of the previous subsection, we can show that the nontrivial fixed points (i.e., $\pm q1$) are unstable for any $\tau \geq 0$. For the trivial fixed point (i.e., $x^* = 0$), we can derive the following equations:

$$J_0 = -a, \quad \text{and} \quad J_\tau = -b_1[-n + ml]. \tag{2.27}$$

Now, the *characteristic equation* is given by

$$\lambda = -a - b_1[-n + ml]e^{-\lambda\tau}. \tag{2.28}$$

Stability for $\tau = 0$ can be found as $a > -b_1[-n + ml]$. Also, for $\tau \neq 0$, from the condition $|J_\tau| \geq |J_0|$, we have the condition of stability: $\left|b_1[-n+ml]\right| \geq |-a|$. Next, similar as the previous section, we can have the set of curves from the expressions of τ_{k1} and τ_{k2} given by Eq. (2.17) with the values of J_0 and J_τ given by Eq. (2.27). These set of curves are shown in Fig. 2.3. We can show that Eq. (2.22) holds good for negative b also; thus, we conclude that, for negative b, the stability zone lies between the curves $\tau = 0$ and τ_{01} in the figure.

To test the validity of our analysis, let us use the following parameter values: $a = 1$, $n = 2.2$, $m = 1$, and $l = 10$. For $b = -1$, we get $J_0 = -a = -1$ and $J_\tau = -b_1[-n + ml\ \text{sech}^2(lx^*)] = -7.8$ ($x^* = 0$). Thus, we see that $|J_\tau| > |J_0|$ (satisfying Eq. (2.11)). Also, at these parameter values, we have $\tau_{01} = 0.22$ (from Eq. (2.17)). Thus, we expect that at $b = -1$ and $\tau_{01} = \tau_H = 0.22$, the fixed point losses its stability through Hopf bifurcation. Further, at these parameter values, we have $g_{11} = g_{20} = g_{02} = 0$, $g_{21} = -184.934 - 99.586i$, $E_1 = E_2 = 0$, $W_{20} = W_{11} = 0$, and $c_1(0) = -92.467 - 49.793i$. Using these set of values in Eq. (2.25), we have $\mu_2 = 6.761 > 0$; that means the resulting bifurcation is a *supercritical* Hopf bifurcation. Also, $\beta_2 = -184.934 < 0$ indicates that the bifurcating periodic

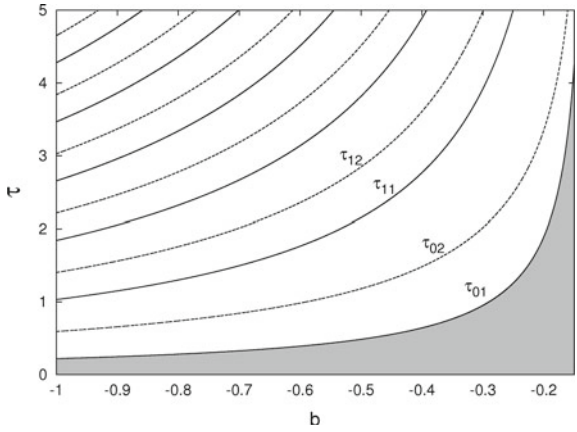

Fig. 2.3 Stability zone in the b–τ ($b < 0$) parameter space with parameters $a = 1$, $n = 2.2$, $m = 1$, and $l = 10$. Shaded region indicates the zone of stable fixed point

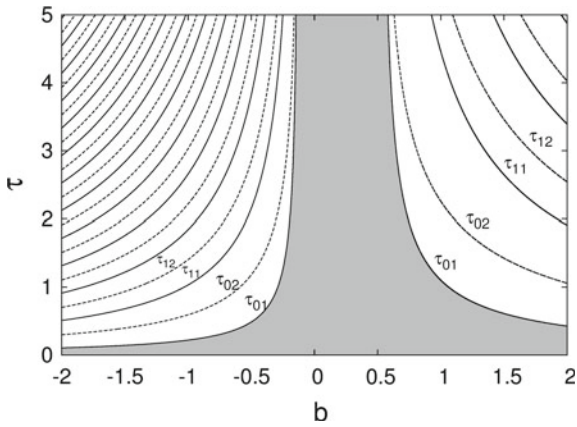

Fig. 2.4 Full stability diagram in $b - \tau$ space, with parameters $a = 1$, $n = 2.2$, $m = 1$, and $l = 10$. The shaded region represents the zone of stable fixed point

solutions are orbitally asymptotically stable. Finally, we have $T_2 = 28.635 > 0$; thus, the period of the limit cycle increases with increasing τ. To sum up the whole scenario of the stability, we present the stability diagram in $b - \tau$ space in Fig. 2.4. The shaded region in the figure represents the zone of stable fixed points of the system.

2.3 Numerical Studies

System Eq. (2.1) is solved numerically using XPPAUT [35] with the fourth-order Runge–Kutta algorithm with step size $h = 0.005$. A constant initial function $\phi(t) = 0.8$ for $t \in [-\tau, 0]$ is used. We also verify that several other initial functions also give similar results. Care has been taken to allow the system to settle to the steady state by excluding a large number of transients.

2.3.1 *Varying* τ *with Constant* b

At first, we vary the time-delay τ with constant b. For all the numerical simulations, we consider the following system parameters: $a = 1, n = 2.2, m = 1$, and $l = 10$. As suggested by the stability diagram Fig. 2.4, in the following, we take two exemplary values of b: $b = 1$ and $b = -1$.

(i) $b = 1$: For $\tau \geq 1.102$, the fixed point loses its stability through Hopf bifurcation, which is in accordance with analysis of the previous section. At $\tau = 1.65$, limit cycle of period-1 becomes unstable and a period-2 (P2) cycle appears. Further, period doubling occurs at $\tau = 1.79$ (P2 to P4). Through a period-doubling sequence, the system enters into the chaotic regime at $\tau = 1.84$. With further increase of τ, at $\tau = 2.60$, the system shows the emergence of hyperchaos. The system shows a double scroll at $\tau \approx 3.24$. Phase-plane representation in the representative $x(t) - x(t - \tau)$ plane for different τ is shown in Fig. 2.5, which shows the following characteristics: period-1 ($\tau = 1.40$), period-2 ($\tau = 1.72$), chaos ($\tau = 1.94$), and double-scroll hyperchaos ($\tau = 3.52$).

(ii) $b = -1$: The fixed point loses its stability through Hopf bifurcation at $\tau = 0.22$ which again agrees with the analysis. Pitchfork bifurcation of the limit cycle occurs at $\tau = 1.3$. Period-2 and period-4 occurs at $\tau = 1.84$ and 1.99, respectively. Chaos appears at $\tau \approx 2.05$. Double scroll occurs at $\tau \approx 2.38$. Finally, hyperchaos occurs at $\tau \approx 3.39$. All the behaviors in phase space are

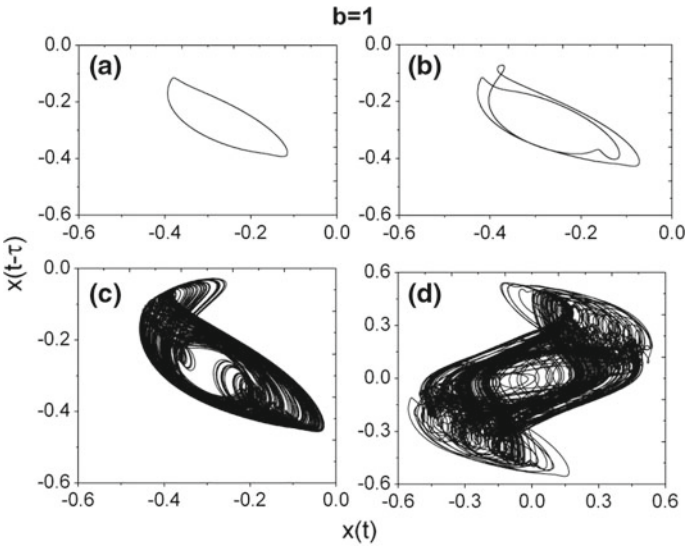

Fig. 2.5 Phase-plane plot in $x(t)$–$x(t - \tau)$ space for different τ ($b = 1$): **a** $\tau = 1.40$ (period-1), **b** $\tau = 1.72$ (period-2), **c** $\tau = 1.94$ (chaos), **d** $\tau = 3.52$ (double-scroll hyperchaos) (other parameters are $a = 1$, $n = 2.2$, $m = 1$, and $l = 10$)

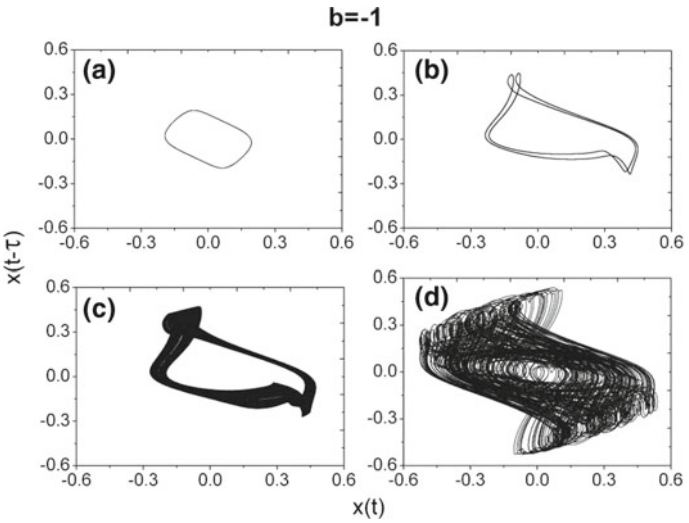

Fig. 2.6 Phase-plane plot in x–$x(t-\tau)$ space for different τ ($b = -1$): **a** $\tau = 0.52$ (period-1), **b** $\tau = 1.876$ (period-2), **c** $\tau = 2.17$ (chaos), **d** $\tau = 3.5$ (double-scroll hyperchaos) (other parameters are $a = 1$, $n = 2.2$, $m = 1$, and $l = 10$)

shown in Fig. 2.6. The representative real-time plots of the system for $b = 0.96$ and $b = -0.96$ with $\tau = 4$ is shown in Fig. 2.7.

These observations are summarized through a bifurcation diagram with τ as the control parameter. Bifurcation diagrams are obtained by plotting the local maxima of x, excluding a large number of transients ($\sim 10^6$). Figure 2.8A(a) and B(a) shows the bifurcation diagram of x with τ for $b = 1$ and $b = -1$, respectively. Clearly, they show a period-doubling route to chaos. For quantitative measure of the system dynamics, we compute the first eight Lyapunov exponents using the algorithm proposed in [37]. Figure 2.8A(b) and B(b) shows the spectrum of Lyapunov exponents (LEs) in the τ parameter space. They agree well with the bifurcation diagrams. Figure 2.8A(c), B(c) show the corresponding Kaplan–Yorke dimensions (D_{KY}) with different τ. The presence of a strange attractor, multiple LEs, and higher values of D_{KY} (> 3) ensures [72] that hyperchaos occurs for $\tau \approx 2.68$ ($b = 1$) and $\tau \approx 3.25$ ($b = -1$).

2.3.2 *Varying* b *with Constant* τ

Next, we keep the delay fixed at $\tau = 4$ and vary b to explore the system dynamics.

(i) $b > 0$: Starting from $b = 0$, if we increase b, at $b \approx 0.128$, the trivial fixed point $x = 0$ losses stability through pitchfork bifurcation and nontrivial fixed points

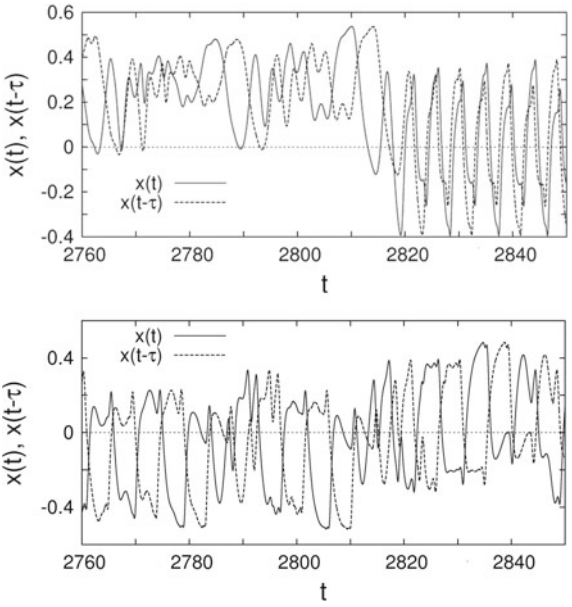

Fig. 2.7 Real-time plot in $x, x(t-\tau) - t$ for $b = 0.96$ (upper panel) and $b = -0.96$ (lower panel), $\tau = 4$ (other parameters are $a = 1$, $n = 2.2$, $m = 1$, and $l = 10$)

arise. Nontrivial fixed points become unstable through Hopf bifurcation and limit cycle appears at $b \approx 0.62 = b_{H+}$. At $b \approx 0.75$, limit cycle of period-1 becomes unstable and a period-2 (P2) cycle appears. Further, period doubling occurs at $b \approx 0.777$ (P2 to P4). Through a period-doubling cascade, the system enters into the chaotic regime at $b \approx 0.786$. With further increase in b, at $b \approx 0.9$, the system shows the hyperchaotic behavior. Double scroll appears at $b \approx 0.985$. Finally, the system equation shows diverging behavior for $b > 1$, indicating boundary crises.

(ii) $b < 0$: For $b \leq -0.156$, the trivial fixed point losses stability through Hopf bifurcation and gives birth to a limit cycle. Pitchfork bifurcation of limit cycle is observed at $b \approx -0.62$. Period-2 limit cycle appears at $b \approx -0.77$, and period-4 oscillation occurs at $b \approx -0.795$. At $b \approx -0.807$, we observe chaotic behavior. Double scroll hyperchaos is observed at $b \approx -0.98$. Phase-plane representation in the representative $x(t) - x(t-\tau)$ plane for different b is shown in Fig. 2.9, which shows the following characteristics: period-1 ($b = 0.70$), period-2 ($b = 0.76$), chaos ($b = 0.82$), and double scroll ($b = 0.99$); period-1 ($b = -0.2$), period-2 ($b = -0.78$), chaos ($b = -0.82$), and double scroll hyperchaos ($b = -1$).

As before, these observations are summarized through a bifurcation diagram with b as the control parameter. Figure 2.10a shows the bifurcation diagram of x with b. At $b_{H+} = 0.62$ and $b_{H-} = -0.156$, limit cycles emerge through Hopf bifurcation. Figure 2.10b shows the first eight LEs; it can be seen that for $b > 0.9$ and $b < -0.93$ we have two positive LEs indicating the occurrence of hyperchaos. This fact is

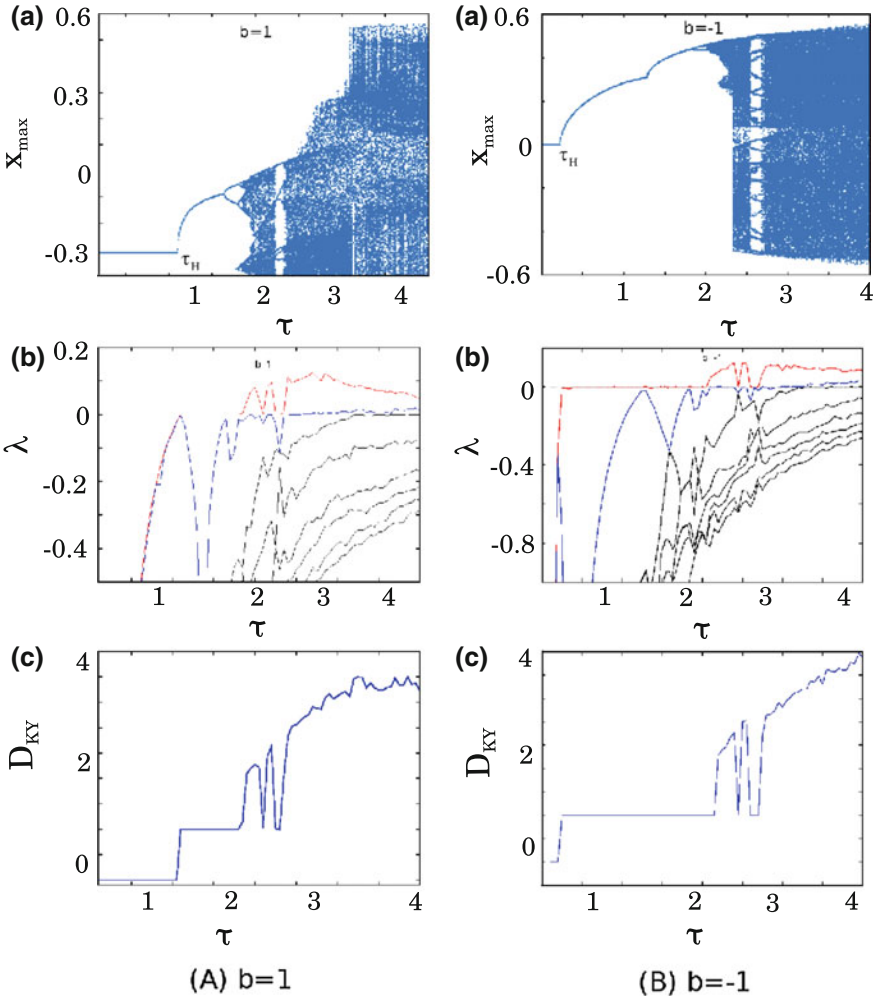

Fig. 2.8 (A) $b = 1$:**a** Bifurcation diagram of x with τ as the control parameter. τ_H indicates the Hopf bifurcation point. **b** The first eight Lyapunov exponents (λ) with τ; First two LEs become positive for $\tau \geq 2.68$ indicating hyperchaos. **c** The corresponding Kaplan–Yorke dimension (D_{KY}).(B) $b = -1$: **a** Bifurcation diagram of x with τ as the control parameter. **b** The first eight Lyapunov exponents (λ) with τ; First two LEs become positive for $\tau \geq 3.25$ indicating hyperchaos. **c** The corresponding Kaplan–Yorke dimension (D_{KY}) (other parameters are same as in Fig. 2.5)

supported by Fig. 2.10c, which plots D_{KY} with b. It is noteworthy that to obtain hyperchaos we do not need to make τ large; a suitable choice of b with a moderate value of τ is sufficient to observe hyperchaos.

It is interesting to note that the nonlinearity of the system solely depends on the control parameters n, m, and l (see Fig. 2.1). The variation of these parameters changes the structure of the nonlinearity but the nature of the nonlinearity is kept

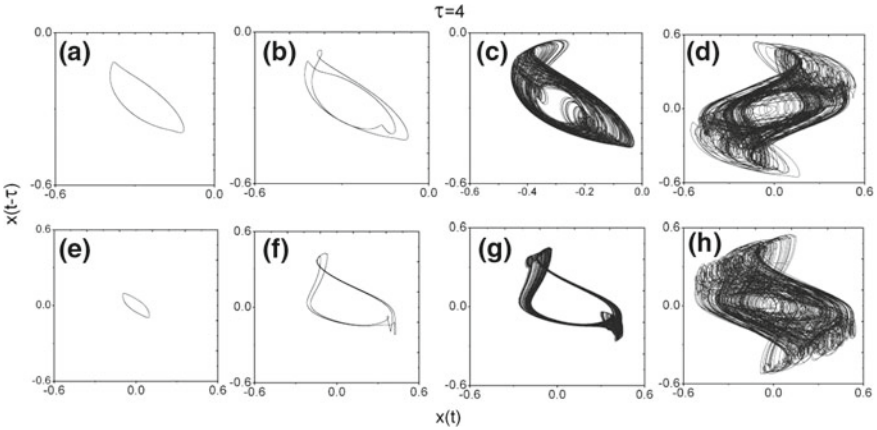

Fig. 2.9 Phase-plane plot in $x(t)$–$x(t-\tau)$ space for different b ($\tau = 4$): **a** $b = 0.7$ (period-1), **b** $b = 0.76$ (period-2), **c** $b = 0.82$ (chaos), **d** $b = 0.99$ (double scroll hyperchaos), **e** $b = -0.2$ (period-1), **f** $b = -0.78$ (period-2), **g** $b = -0.82$ (chaos), and **h** $b = -1$ (double scroll) (other parameters are $a = 1$, $n = 2.2$, $m = 1$, and $l = 10$)

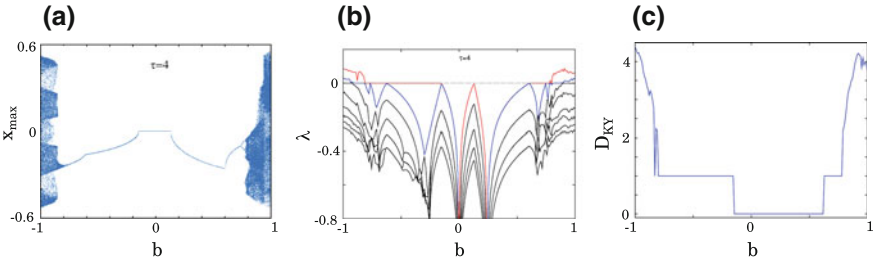

Fig. 2.10 **a** Bifurcation diagram of x with b as the control parameter. **b** The first eight Lyapunov exponents (λ) with b; First two LEs become positive for $b \geq 0.9$ and $b \leq -0.92$ indicating hyperchaos. **c** The corresponding Kaplan–Yorke dimension (D_{KY}). Parameter values are same as in Fig. 2.9

unaltered by keeping the condition $n < ml$ to have the double hump in the nonlinearity. In Fig. 2.11, we show the resulting forms of nonlinearity under the variation of each parameter by different shaded colors. The range of parameters is as follows: $n \in [1, 2.4]$ (cyan zone in Fig. 2.11), $m \in [0.5, 1.5]$ (yellow zone in Fig. 2.11), and $l \in [3, 12]$ (red zone in Fig. 2.11). Other parameters are $n = 2.2$, $m = 1$, and $l = 10$ if they are not used as control parameters. It is interesting to note that the change in the form of the nonilearity is also responsible to show the full spectrum of system dynamics.

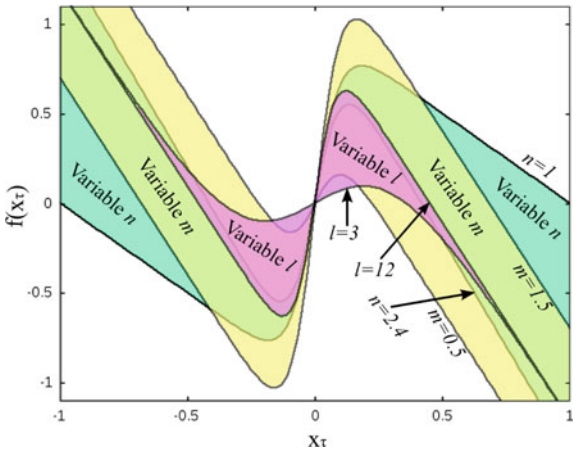

Fig. 2.11 Nonlinear zones for variable control parameters. $n \in [1, 2.4]$ (cyan zone), $m \in [0.5, 1.5]$ (yellow zone), and $l \in [3, 12]$ (red zone). Solid lines are for the parameters $n = 2.2$, $m = 1$, and $l = 10$

2.4 Experimental Studies

The system given by Eq. (2.1) (with the nonlinearity of Eq. (2.2)) is implemented in an analog electronic circuit as shown in Fig. 2.12. Here, $V(t)$ represents the voltage drop across the capacitor C_0 of the low-pass filter section $R_0 - C_0$. Figure 2.12 follows the following circuit equation:

$$R_0 C_0 \frac{dV(t)}{dt} = -V(t) + bf\big(V(t - T_d)\big). \tag{2.29}$$

Here, $b = \pm\frac{R_7}{R_6}$. Positive (negative) sign is considered if the junction "P" is connected to "A" ("B"). A4 is an unity gain inverting amplifier (i.e., $R_8 = R_9$). A5 and A6 are noninverting unity gain amplifiers acting as voltage buffers. $f\big(V(t - T_d)\big) \equiv f(V_\tau)$ is the nonlinear function representing the output of the nonlinear device (ND) of Fig. 2.12 in terms of the input voltage V_τ. T_D is the time delay produced by a delay block.

Figure 2.12 shows that ND consists of the following parts: The circuit associated with the A1 op-amp is a simple inverting amplifier of gain $\frac{R_2}{R_1}$. The output is a linear function of the input for a certain range of input voltage; for a higher input voltage, the output is saturated to a constant, $\pm V_{sat}$, which is the saturation voltage of op-amp. This nature of the op-amp-based amplifier can best be represented by the following function: $-\beta V_{sat} \tanh\left(w\frac{R_2}{R_1}\frac{V_\tau}{V_{sat}}\right)$. We chose a $\tanh(\cdot)$ function to represent a saturation-type nonlinearity because this particular function is widely considered in bipolar and CMOS IC design. Here, β and w are the scaling factors needed to fit the model with the experimental data; these two parameters depend upon the nonideal nature and asymmetry of the op-amps. In general, for smaller input voltages, $\beta \approx 1$ and $w \approx 1$. A2 acts as a weighted adder that adds V_τ and the output voltage of A1.

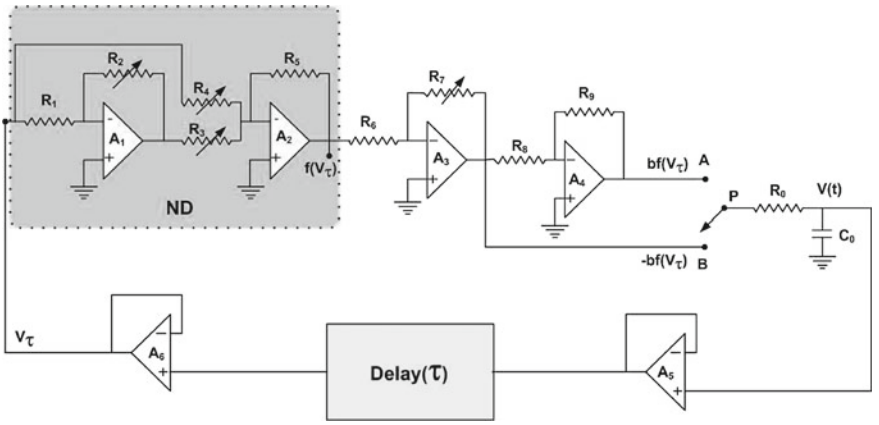

Fig. 2.12 Experimental circuit diagram. ND is the nonlinear device. A1–A6 are op-amps (TL074); low-pass section has $R_0 \approx 1\text{k}\Omega$ and $C_0 \approx 0.1\ \mu$F. For ND: $R_1 \approx 2.50$ kΩ, $R_2 \approx 20.23$ kΩ, $R_3 \approx 26.28$ kΩ, $R_4 \approx 8.71$ kΩ, $R_5 \approx 10$ kΩ. $R_6 \approx 1$ kΩ, and variable POT for R_7. Other resistors are $R_8 = R_9 \approx 10$ kΩ. Delay block contributes a delay of τ (see Fig. 2.13)

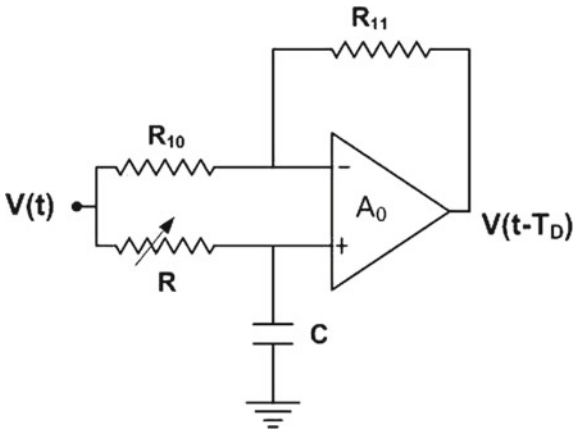

Fig. 2.13 Active first-order all-pass filter. A_0 is a TL074 op-amp. $R_{10} = R_{11} \approx 2.2$ kΩ, $C \approx 10$ nF

Therefore, we can write the following form of the nonlinearity:

$$f\big(V(t-T_D)\big) = -\frac{R_5}{R_4}V(t-T_D) + \frac{R_5}{R_3}\beta V_{sat}\tanh\left(w\frac{R_2}{R_1}\frac{V(t-T_D)}{V_{sat}}\right). \quad (2.30)$$

The variable delay element is realized by the first-order *all-pass filter* (APF) (Fig. 2.13) [115]. Design of an APF needs a single op-amp (A_0), an $R-C$ combination, which determines the phase shift between the input and output signals; two resistors R_{10} and R_{11} determine the gain of the APF. Thus, the APF has the following transfer function:

$$T(s) = -a_1 \frac{s - \omega_0}{s + \omega_0}, \tag{2.31}$$

with a flat gain $a_1 = \frac{R_{11}}{R_{10}}$, and $\omega_0 = 1/CR$ is the frequency at which the phase shift is $\pi/2$. In the present work, we take $R_{11} = R_{10}$, and thus $a_1 = 1$. Since it has a maximally linear phase response around the frequency ω_0, thus one can approximate that an APF imposes a delay of $T_D \approx RC$ around ω_0 [13]. Thus, i blocks produce a delay of $T_D \approx iRC$ ($i = 1, 2, \ldots$). By simply changing the resistance R, one can vary the amount of delay; thus, one can control the resolution of the delay line easily.

Let us define the following dimensionless variables and parameters: $t = \frac{t}{R_0 C_0}$, $\tau = \frac{T_d}{R_0 C_0}$, $x = \frac{V(t)}{V_{sat}}$, $x_\tau = \frac{V(t-T_D)}{V_{sat}}$, $\frac{R_5}{R_4} = n_1$, $\beta \frac{R_5}{R_3} = m_1$, and $w \frac{R_2}{R_1} = l_1$. Now, the system Eq. (2.29) can be reduced to the following dimensionless first-order, nonlinear delay differential equation:

$$\frac{dx}{dt} = -x(t) + bf\big(x(t-\tau)\big), \tag{2.32}$$

where

$$f\big(x(t-\tau)\big) \equiv f(x_\tau) = -n_1 x_\tau + m_1 \tanh(l_1 x_\tau). \tag{2.33}$$

It can be seen that Eq. (2.32) (along with Eq. (2.33)) is equivalent to Eq. (2.1) (along with Eq. (2.2)) with $a = 1$, and appropriate choice of n_1, m_1, and l_1.

In the hardware experiment, we use IC TL074 (quad JFET op-amp) with ± 12 volt power supply. Capacitors (resistors) have 1% (5%) tolerance. For the low-pass section, we choose $R_0 \approx 1$ kΩ and $C_0 \approx 0.1$ μF. For the nonlinear device (ND), the following resistor values are used: $R_1 \approx 2.50$ kΩ, $R_2 \approx 20.23$ kΩ, $R_3 \approx 26.28$ kΩ, $R_4 \approx 8.71$ kΩ, and $R_5 \approx 10$ kΩ. Figure 2.14 shows the experimentally obtained nonlinearity produced by the ND. Qualitatively, it is equivalent to the nonlinear function "N1" of Fig. 2.1. The gain of the noninverting amplifier (A3) that follows the ND is designed with $R_6 \approx 1$ kΩ and variable R_7; R_7 is varied through a potentiometer to change the parameter b. Other resistors are $R_8 \approx 10$ kΩ and $R_9 \approx 10$ kΩ. For the delay section, the APF is designed with the following parameters: $R \approx 10$ kΩ

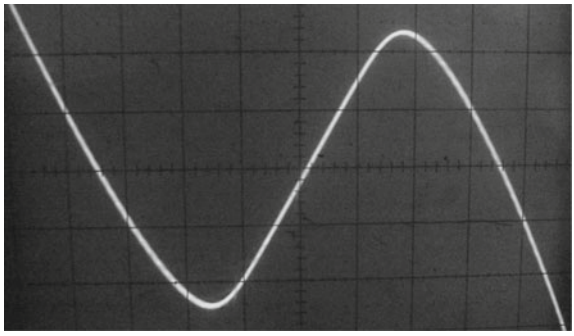

Fig. 2.14 Experimentally obtained nonlinearity produced by nonlinear device of Fig. 2.12. Scale: x-axis: 0.2 v/div and y-axis: 0.5 v/div

(POT), $C \approx 10$ nF, $R_8 \approx 2.2$ kΩ, and $R_9 \approx 2.2$ kΩ. Each APF contributes a delay of $T_D = RC = 0.1$ ms; thus, the dimensionless parameter $\tau = \frac{RC}{R_0 C_0} = 1$, i.e., one needs i blocks to produce a delay $\tau = i$. In the experiment, we vary R to get variable delays. Note that one can also change R_0 to get a variable delay, but in that case the power spectral property of the circuit will also be changed [89].

2.4.1 *Variable* τ, *Fixed* B

(i) *Positive b*: The nodes "A" and "P" of Fig. 2.12 are connected. We fix the value of b with $R_7 \approx 1.57$ kΩ (POT). Now, we vary the delay by varying R. At first to get a small delay, we use only one APF stage. For $R \geq 9.56$ kΩ (approx.), a stable limit cycle appears with frequency 3846 Hz. Next, we use two blocks of APF; $R \approx 10$ kΩ is taken for the first block (contributing ≈0.1 ms delay) and vary R of the second block; at $R = 0.35$ kΩ the limit cycle of period-1 loses its stability and a period-2 oscillation emerges. At $R \approx 6.43$ kΩ, chaotic oscillation occurs in the circuit. Next, we use three blocks of APF; $R \approx 10$ kΩ is taken for the first two blocks (contributing ≈ 0.2 ms delay) and vary R of the third block; the double-scroll hyperchaotic attractor is observed beyond $R \approx 6.84$ kΩ. All the above-mentioned behaviors are shown in Fig. 2.15 (in $V(t)$–$V(t - T_D)$ space), which depicts the experimental phase-plane plots recorded in a real-time oscilloscope (Aplab make, two channel, 60 MHz). It can be seen that the experimental results qualitatively agree well with the numerical simulations.

(ii) *Negative b*: The nodes "B" and "P" of Fig. 2.12 are connected. We fix the value of b with $R_7 = 1.56$ kΩ (POT). The following observations are made: period-1 (frequency 7692 Hz) is observed for single stage, $R \geq 9$ kΩ. Next, we use three blocks of APF: $R \approx 10$ kΩ is taken for the first two blocks (contributing ≈ 0.2 ms delay) and vary R of the third block. The following behaviors are observed: period-2 ($R \geq 2.77$ kΩ), chaos ($R \geq 4.09$ kΩ), and double scroll ($R \geq 9.54$ kΩ). Oscilloscope traces are shown in Fig. 2.16.

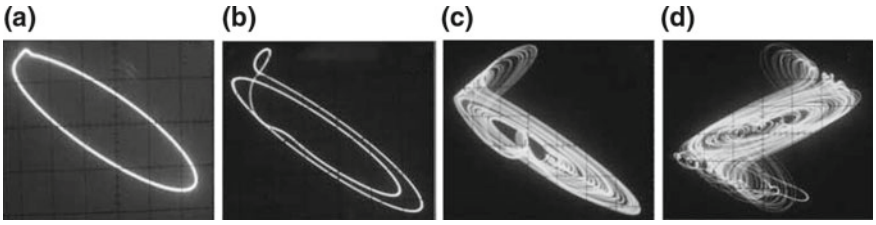

Fig. 2.15 Positive b: The oscilloscope trace of experimentally obtained phase-plane plots in the $V(t)$–$V(t - T_D)$ space for variable τ: **a** Period-1 **b** Period-2 **c** chaos **d** double scroll (for the parameter values see text). **a–c** V (x-axis): 0.2 v/div, $V(t - T_D)$ (y-axis): 0.2 v/div. **d** x-axis: 0.5 v/div, y-axis: 0.5 v/div

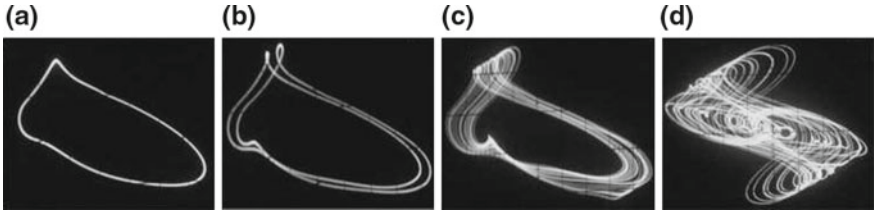

Fig. 2.16 Negative b: The oscilloscope trace of experimentally obtained phase-plane plots in the $V(t)$–$V(t - T_D)$ space for variable τ: **a** Period-1 **b** Period-2 **c** chaos **d** double scroll (for the parameters see text). **a**–**d** x-axis: 0.5 v/div, y-axis: 0.5 v/div

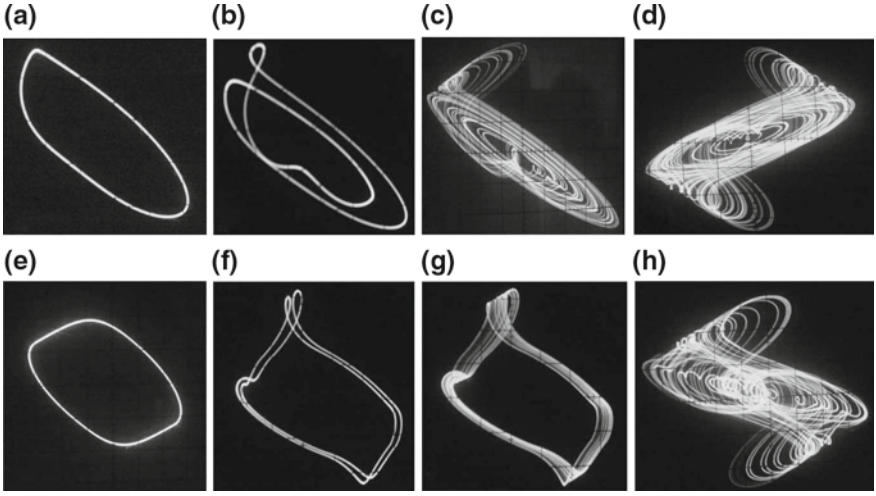

Fig. 2.17 The oscilloscope trace of experimentally obtained phase-plane plots in the $V(t)$–$V(t - T_D)$ space for variable b: "A"–"P" (of Fig. 2.12) are connected (positive b): **a** Period-1 at $R_7 = 1.01$ kΩ **b** Period-2 at $R_7 = 1.12$ kΩ **c** chaos at $R_7 = 1.3$ kΩ **d** double scroll at $R_7 = 1.7$ kΩ. "B"–"P" (of Fig. 2.12) are connected (negative b): **e** Period-1 at $R_7 = 0.75$ kΩ **f** Period-2 at $R_7 = 1.12$ kΩ **g** chaos at $R_7 = 1.30$ kΩ **h** double scroll at $R_7 = 1.45$ kΩ (for other parameters see text). **a**–**c** x-axis: 0.1 v/div, y-axis: 0.2 v/div. **d** x-axis: 0.5 v/div, y-axis: 0.5 v/div., and **e**–**g** x-axis: 0.1 v/div, y-axis): 0.2 v/div.; **h** x-axis: 0.5 v/div, y-axis: 0.5 v/div

2.4.2 *Variable* B, *Fixed* τ

(i) *Positive b*: The nodes "A" and "P" of Fig. 2.12 are connected. We set the time delay at $T_D = 0.4$ ms (i.e., $\tau = 4$) by using four APF blocks each having $R = 10$ kΩ. To observe the behavior of the system for different b, we vary R_7. For $R_7 \approx 1$ kΩ (i.e., $b = 1$), the circuit shows a stable limit cycle of frequency 833 Hz. At $R_7 = 1.07$ kΩ (approx.) (i.e., $b \approx 1.07$), the limit cycle of period-1 loses its stability and a period-2 oscillation emerges. Chaotic oscillation appears at $R_7 = 1.17$ kΩ (approx.) (i.e., $b \approx 1.17$). The circuit shows a double scroll for $R_7 > 1.61$ kΩ (i.e., $b \approx 1.61$). These behaviors are shown in Fig. 2.17

(upper row (a)–(d)) which represents the experimental oscilloscope traces in the $V(t) - V(t - T_D)$ space. One can observe the *qualitative* agreement between the numerical results and the experimental observations.

(ii) *Negative b*: The nodes "B" and "P" of Fig. 2.12 are connected. We set the time delay at $T_D = 0.4$ ms (i.e., $\tau = 4$). Following observations are made: period-1 ($R_7 \geq 0.67$ kΩ, $b = 0.67$), period-2 ($R_7 \geq 1.08$ kΩ, $b = 1.08$), chaos ($R_7 \geq 1.09$ kΩ, $b = 1.09$), and double scroll ($R_7 \geq 1.43$ kΩ, $b = 1.43$). All the above- mentioned behaviors are shown in Fig. 2.17 (lower row (e)–(h)) in $V(t)$–$V(t - T_D)$ space depicting the real-time oscilloscope traces. Thus, we see that the experimental results *qualitatively* agree well with the numerical results.

2.5 Time-Delayed System with Unimodal Nonlinearity: System Description

Next, we discuss the design principle of a chaotic time-delayed system with unimodal nonlinearity. The following is the first-order nonlinear retarded-type delay differential equation with a single constant delay

$$\dot{x} = -ax(t) - bf(x_\tau), \tag{2.34}$$

where a and b are the positive parameters. Also, $x_\tau \equiv x(t - \tau)$, where $\tau \in \mathscr{R}^+$ is a constant time delay. The nonlinear function of the above equation is given by the following equation:

$$f(x_\tau) = -0.5n\big(|x_\tau| + x_\tau\big) + m\tanh(lx_\tau), \tag{2.35}$$

where n, m, and l are all positive parameters controlling the nonlinearity.

The first term in the right-hand side of Eq. (2.35) represents the input–output characteristic of a half-wave (HW) rectifier. Thus, the nonlinear function is composed of the weighted superposition of two nonlinear functions, namely "HW" and "tanh(·)" functions. Figure 2.18 shows the nature of the nonlinearity for different values of n, m, and l. The nonlinearity shows a unimodal nature with single hump in the first quadrant, but unlike the nonlinearity of the Mackey–Glass (MG) system [79], it does not vanish asymptotically. There exists a large number of choices of n, m, and l that produce this particular nature of the nonlinearity.

2.6 Stability Analysis

To analyze the stability of the system given by Eq. (2.34), we rewrite it in the following form:

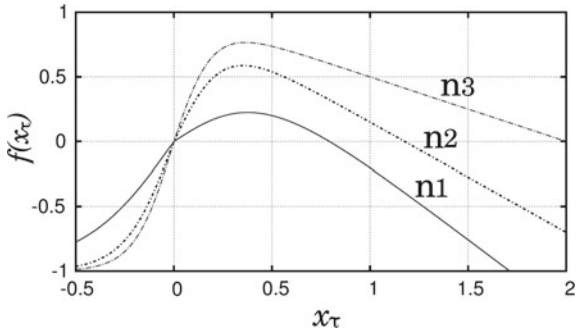

Fig. 2.18 Nonlinear function $f(x_\tau) = -0.5n(|x_\tau| + x_\tau) + m\tanh(lx_\tau)$: (n1) $n = 1.15$, $m = 0.97$, $l = 2.19$; (n2) $n = 0.85$, $m = 1$, $l = 4$; (n3) $n = 0.5$, $m = 1$, and $l = 5$

$$\dot{x} = g\Big(x(t), x_\tau\Big) = -ax(t) - bf(x_\tau). \tag{2.36}$$

The equilibrium condition implies $\dot{x} = 0$ and $x(t) = x_\tau = x^*$ (say), i.e., $g(x^*, x^*) = -ax^* - bf(x^*) = 0$. This gives $ax^* = -bf(x^*)$. This is a *transcendental equation*, which may be solved graphically (or numerically, e.g., Newton–Raphson method). The intersection of the two curves gives the solution, which is $x^* = 0$. Let us now examine the stability of the fixed point $x^* = 0$.

The analysis of stability is same as in Sect. 2.2. The condition of stability for $\tau = 0$ is given by

$$b\Big[-0.5n + ml\Big] > -a. \tag{2.37}$$

The stability condition for $\tau \neq 0$ gives the calculated values of τ as

$$\tau_{k1} = \frac{\Big[\cos^{-1}\Big(-\frac{J_0}{J_\tau}\Big) + 2k\pi\Big]}{\sqrt{{J_\tau}^2 - {J_0}^2}}, \qquad \text{for } J_\tau < 0, \tag{2.38a}$$

$$\tau_{k2} = \frac{\Big[\Big\{2\pi - \cos^{-1}\Big(-\frac{J_0}{J_\tau}\Big)\Big\} + 2k\pi\Big]}{\sqrt{{J_\tau}^2 - {J_0}^2}}, \qquad \text{for } J_\tau > 0, \tag{2.38b}$$

where $k = 0, 1, 2, \ldots$, and J_0 and J_τ are the same as Eqs. (2.6) and (2.7).

The condition of stability of the system reads the following form:

$$\big| - b(0.5n - ml)\big| \geq |-a|. \tag{2.39}$$

Also, we get the derivative of the real part of the eigenvalue as

$$\mu'(\tau_k) = \frac{{\nu_0}^2}{(1 + \tau_k a)^2 + \tau_k^2 \nu_0^2}. \tag{2.40}$$

Thus, $\mu'(\tau_k) > 0$ for any $k = 0, 1, 2, \ldots$. Thus, we conclude that the stable state lies between $\tau = 0$ and τ_{01}.

Figure 2.19 shows the first six stability curves τ_{ki} $(i = 1, 2)$ (using Eqs. (2.38a) and (2.38b)) in the $b - \tau$ parameter space. We have used the following parameters: $a = 1$, $n = 1.15$, $m = 0.97$, and $l = 2.19$ (as we have used in "n1" of Fig. 2.18). In the figure, τ_{k1} and τ_{k2} are represented by the solid and dotted lines, respectively. Since $\mu(\tau_k) > 0$ for any $k = 0, 1, 2, \ldots$, thus the stability zone cannot be situated between two τ_{ki} curves; so we conclude that the stable island lies between the $\tau = 0$ and the τ_{01} curve. The shaded region in the figure represents the stable zone, and the τ_{01} curve represents the Hopf bifurcation curve.

Further, we analyze the stability of the system using TRACE-DDE package in which *pseudospectral approach* is considered [23]. The package is employed for the calculation of stability zone. In Fig. 2.20a, we show the stability boundary and in Fig. 2.20b the stability surface. This figure closely resembles our analytically obtained results as shown in Fig. 2.19.

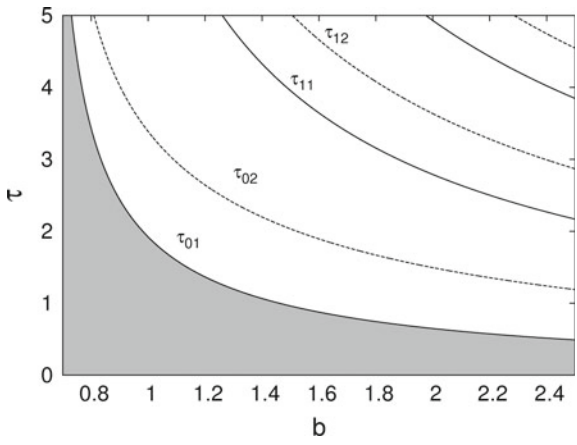

Fig. 2.19 Stability zone in the $b - \tau$ parameter space with parameters $a = 1$, $n = 1.15$, $m = 0.97$, and $l = 2.19$. The shaded region indicates the zone of the stable fixed point

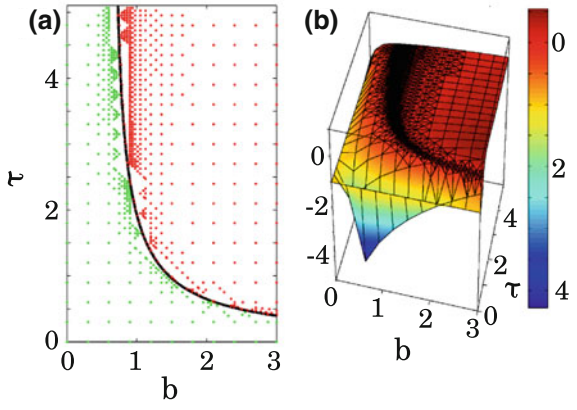

Fig. 2.20 Stability zone in $b - \tau$ parameter space obtained by the numerical package TRACE-DDE: **a** Stability boundary and **b** Stability surface. The parameters are same as in Fig. 2.19

From the aforesaid discussion, it is clear that the system undergoes a Hopf bifurcation to loose its stability. Now, we want to find out the type of Hopf bifurcation occurring in the system and also its stability. For this, we consider the stability and direction of hopf bifurcation as discussed in Sect. 2.2.1. The outcomes of the analysis are as follows: To test the validity of our analysis, let us use the following parameter values: $a = 1$, $n = 1.15$, $m = 0.97$, and $l = 2.19$. For $b = 1.7$, we get $J_0 = -a = -1$ and $J_\tau = -b[-0.5n + ml] = -2.634$. Thus, we see that $|J_\tau| \geq |J_0|$ (satisfying Eqs. (2.37) and (2.39)). Also, at these parameter values, we have $\tau_{01} = 0.805$ (from Eq. (2.38a)). Thus, we expect that at $b = 1.7$ and $\tau_{01} = \tau_H = 0.805$, the fixed point losses its stability through Hopf bifurcation. Further, at these parameter values, we have $g_{11} = g_{20} = g_{02} = 0$, $g_{21} = -9.809 - 3.632i$, $E_1 = E_2 = 0$, $W_{20} = W_{11} = 0$, and $c_1(0) = -4.904 - 1.816i$. Using these set of values in Eq. (2.25), we have $\mu_2 = 5.864 > 0$; that means the resulting bifurcation is a *supercritical* Hopf bifurcation. Also, $\beta_2 = -9.809 < 0$; thus the bifurcating periodic solutions are orbitally asymptotically stable. Finally, since $T_2 = 6.182 > 0$, the period of the limit cycle increases with increasing τ.

2.7 Numerical Studies

The system Eq. (2.34) is integrated numerically using the package XPPAUT [35] (using the fourth-order Runge–Kutta algorithm with a step size $h = 0.005$). We use a constant initial function $\phi(t) = 1$ for $t \in [-\tau, 0]$.

2.7.1 Varying τ *with Constant* b

Guided by the analytical results, at first, we vary the time delay τ keeping b constant at $b = 1.7$. Also, the other parameters are kept at $a = 1$, $n = 1.15$, $m = 0.97$, and $l = 2.19$. We find that for $\tau \geq 0.805$, the fixed point loses its stability through Hopf bifurcation, which is in accordance with the analysis of the previous section. At $\tau \approx 2.23$, limit cycle of period-1 becomes unstable and a period-2 (P2) cycle appears. Further, period doubling occurs at $\tau \approx 2.91$ (P2 to P4) and then at $\tau \approx 3.07$ (P4 to P8). Through a period-doubling sequence, the system enters into the chaotic regime at $\tau = 3.1$. With further increase of τ, at $\tau = 3.60$, the system shows the emergence of hyperchaos.

A phase-plane representation in the representative $x(t) - x(t - \tau)$ plane for different τ is shown in Fig. 2.21, which shows the following characteristics: period-1 ($\tau = 1.90$), period-2 ($\tau = 2.76$), period-4 ($\tau = 2.93$), period-8 ($\tau = 3.07$), chaos ($\tau = 3.17$), hyperchaos ($\tau = 4.78$), and $b = 1.7$.

These observations are summarized through a bifurcation diagram (Fig. 2.22) with τ as the control parameter; clearly, it shows a period-doubling route to chaos. Figure 2.22 (middle panel) shows the spectrum of Lyapunov exponents (LEs) in the

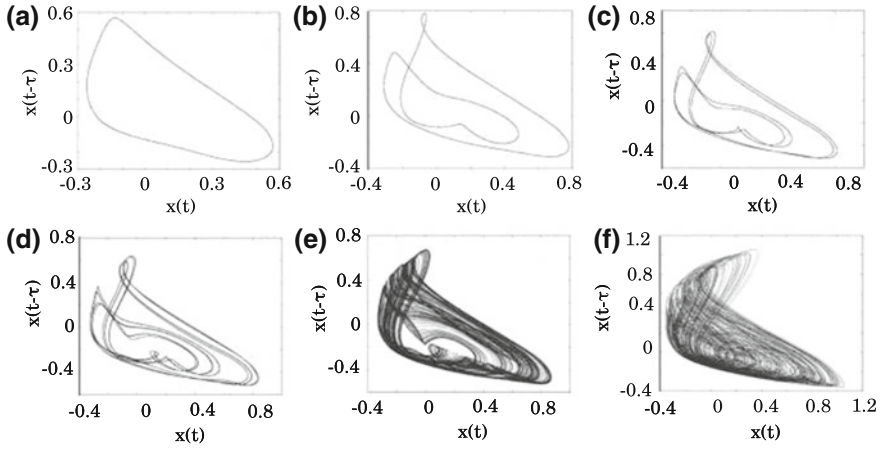

Fig. 2.21 Phase-plane plots in $x - x(t-\tau)$ space for different τ: **a** $\tau = 1.90$ (period-1), **b** $\tau = 2.76$ (period-2), **c** $\tau = 2.93$ (period-4), **d** $\tau = 3.07$ (period-8), **e** $\tau = 3.17$ (chaos), and **f** $\tau = 4.78$ (hyperchaos). Other parameters are $a = 1$, $b = 1.7$, $n = 1.15$, $m = 0.97$, and $l = 2.19$

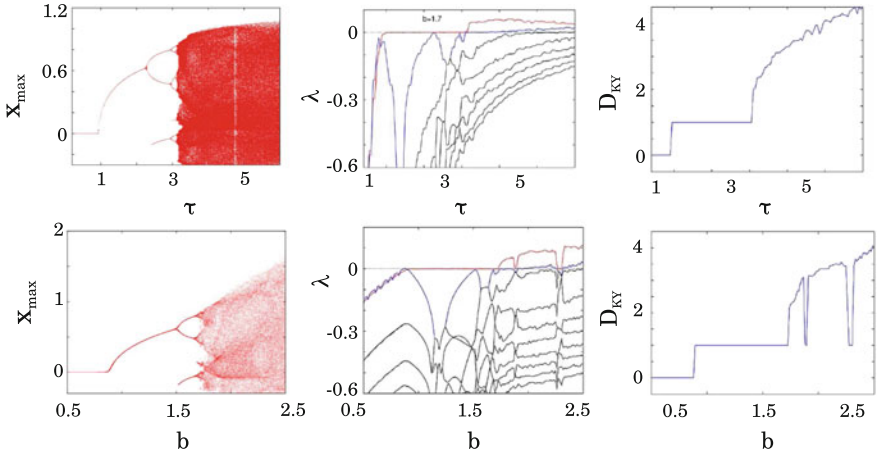

Fig. 2.22 Upper row: Bifurcation diagram of x (*Left panel*) with τ as the control parameter. *Middle* panel shows the first nine Lyapunov exponents (λ) with τ. The first two LEs become positive for $\tau \geq 3.60$, indicating hyperchaos. *Right panel* shows the corresponding Kaplan–Yorke dimension (D_{KY}), ($b = 1.7$). Lower row: Bifurcation diagram of x (*Left panel*) with b as the control parameter. *Middle panel* shows the first ten Lyapunov exponents (λ) with b; the first two LEs become positive for $b \geq 1.9$, indicating hyperchaos. *Right panel* shows the corresponding Kaplan–Yorke dimension (D_{KY}), ($\tau = 3$). Other parameters are $a = 1$, $n = 1.15$, $m = 0.97$, and $l = 2.19$

τ parameter space. The presence of a positive LE *along with the observed strange attractor* and bifurcation diagram indicates the occurrence of a chaotic behavior in the system. Figure 2.22 (right panel) shows the Kaplan–Yorke dimension (D_{KY}) with

different τ. The presence of multiple positive LEs and higher values of $D_{KY}(> 3)$ indicates that hyperchaos occurs for $\tau \geq 3.60$.

2.7.2 *Varying* b *with Constant* τ

Next, we keep the delay fixed at $\tau = 3$ and vary b to explore the system dynamics. It is observed that with increasing b, for $b < 0.834 = b_H$, the system shows a fixed point at $x = 0$. For $b \geq b_H = 0.834$, the fixed point loses its stability through Hopf bifurcation, and a stable limit cycle emerges. This is in well agreement with our analytical results of the previous section. At $b = 1.51$, the limit cycle of period-1 becomes unstable and a period-2 (P2) cycle appears. Further period doubling occurs at $b = 1.68$ (P2 to P4) and at $b = 1.73$ (P4 to P8). Through period-doubling bifurcations, the system enters into the chaotic regime at $b = 1.73$. With further increase of b, at $b = 2.1$, the system shows the emergence of hyperchaos. Finally, the system equation shows diverging behavior beyond $b = 2.52$, indicating boundary crises. A phase-plane representation in the representative $x(t) - x(t - \tau)$ plane for different b is shown in Fig. 2.23, which shows the following characteristics: period-1 ($b = 1.36$), period-2 ($b = 1.64$), period-4 ($b = 1.70$), period-8 ($b = 1.73$), chaos ($b = 1.76$), and hyperchaos ($b = 2.40$).

These observations are summarized through a bifurcation diagram with b as the control parameter Fig. 2.22 (lower row). The observations are further supported by

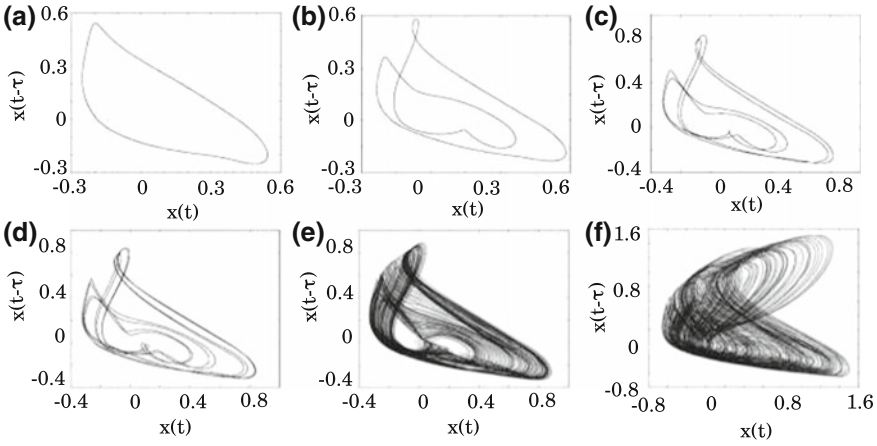

Fig. 2.23 Phase-plane plots in $x - x(t - \tau)$ space for different b: **a** $b = 1.36$ (Period-1), **b** $b = 1.64$ (Period-2), **c** $b = 1.70$ (Period-4), **d** $b = 1.73$ (Period-8), **e** $b = 1.76$ (chaos), and **f** $b = 2.40$ (hyperchaos). Other parameters are $a = 1$, $n = 1.15$, $m = 0.97$, $l = 2.19$, and $\tau = 4$

Fig. 2.22 (right panel), which plots D_{KY} with b. It is noteworthy that to obtain hyperchaos we do not need to make τ high but a suitable choice of b with a moderate value of τ is sufficient.

2.8 Experimental Observations

We implement the system described by Eq. (2.34) using analog electronic circuit. Figure 2.24 shows the representative diagram of the experimental circuit. Let $V(t)$ be the voltage drop across the capacitor C_0 of the low-pass filter section $R_0 - C_0$; thus, the following equation represents the time evolution of the circuit

$$R_0 C_0 \frac{dV(t)}{dt} = -V(t) - \frac{R_7}{R_6} f\big(V(t - T_D)\big), \tag{2.41}$$

where $f\big(V(t - T_D)\big) = f(V_\tau)$ is the nonlinear function representing the output of the nonlinear device (ND) of Fig. 2.24 in terms of the input voltage V_τ. T_D is the time delay produced by the delay block. The different blocks of this figure are illustrated in detail in Figs. 2.25 and 2.13, respectively. The former shows the "ND" part and

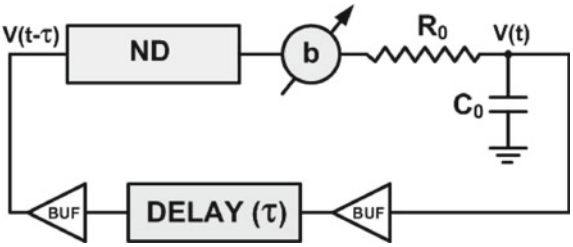

Fig. 2.24 Experimental circuit diagram. $R_0 = 1\,\text{k}\Omega$, $C_0 = 100\,\text{nF}$. Buffers are designed with unity gain noninverting op-amps

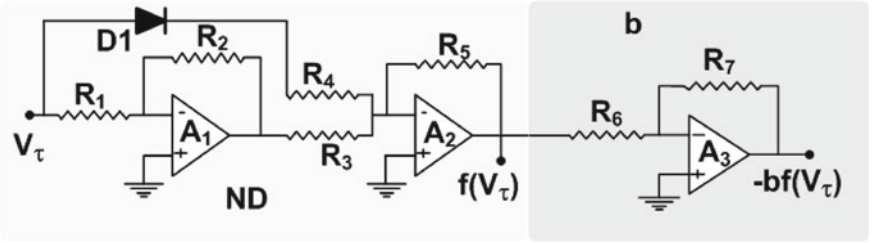

Fig. 2.25 Nonlinear device (ND) along with the amplifying stage (b). A1–A3 are op-amps (TL074), D1 is the diode: 1N4148, $R_1 \approx 10\,\text{k}\Omega$, $R_2 \approx 18.5\,\text{k}\Omega$, $R_3 \approx 12.05\,\text{k}\Omega$, $R_4 \approx 8.25\,\text{k}\Omega$, and $R_5 = R_6 \approx 10\,\text{k}\Omega$

the latter shows the "Delay" part, respectively. We can write the following form of the nonlinearity:

$$f\big(V(t-T_D)\big) = -\frac{R_5}{R_4}0.5\Big[\big|V(t-T_D)\big| + V(t-T_D)\Big] + \frac{R_5}{R_3}\beta V_{sat}\tanh\left(\omega\frac{R_2}{R_1}\frac{V(t-T_D)}{V_{sat}}\right). \tag{2.42}$$

As before, the variable delay element is realized by the first-order all-pass filter (APF) (Fig. 2.13, p. 26).

Let us define the following dimensionless variables and parameters: $t = \frac{t}{R_0C_0}$, $\tau = \frac{T_D}{R_0C_0}$, $x = \frac{V(t)}{V_{sat}}$, $x(t-\tau) = \frac{V(t-\tau)}{V_{sat}}$, $n_1 = \frac{R_5}{R_4}$, $m_1 = \beta\frac{R_5}{R_3}$, and $l_1 = \omega\frac{R_2}{R_1}$. Now, the system Eq. (2.41) can be reduced to the following dimensionless equation:

$$\frac{dx}{dt} = -x(t) - bf\big(x(t-\tau)\big), \tag{2.43}$$

where $b = \frac{R_7}{R_6}$ and

$$f\big(x(t-\tau)\big) \equiv f(x_\tau) = -0.5n_1\big(|x(t-\tau)|+x(t-\tau)\big)+m_1\tanh\big(l_1x(t-\tau)\big). \tag{2.44}$$

It is worth noting that Eq. (2.43) (along with Eq. (2.44)) is equivalent to Eq. (2.34) (along with Eq. (2.35)) with $a = 1$, and appropriate choices of n_1, m_1, and l_1.

For the low-pass section, we choose $R_0 \approx 1$ kΩ and $C_0 \approx 100$ nF. For the nonlinear device (ND), we use a 1N4148 diode; the following resistor values are used: $R_1 \approx 10$ kΩ, $R_2 \approx 18.5$ kΩ, $R_3 \approx 12.05$ kΩ, $R_4 \approx 8.25$ kΩ, and $R_5 \approx 10$ kΩ. Figure 2.26 shows the experimentally obtained nonlinearity produced by the nonlinear device (ND). Qualitatively, it is equivalent to the nonlinear function (n1) of Fig. 2.18. The gain of the noninverting amplifier (A3) that follows the ND part is designed with $R_6 \approx 10$ kΩ and variable R_7; R_7 is varied with a potentiometer to

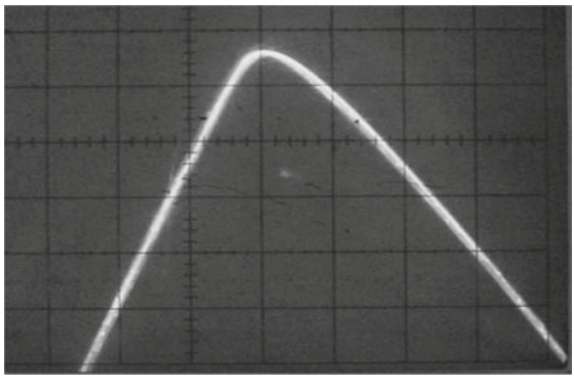

Fig. 2.26 Experimentally obtained nonlinearity produced by the ND part of Fig. 2.25

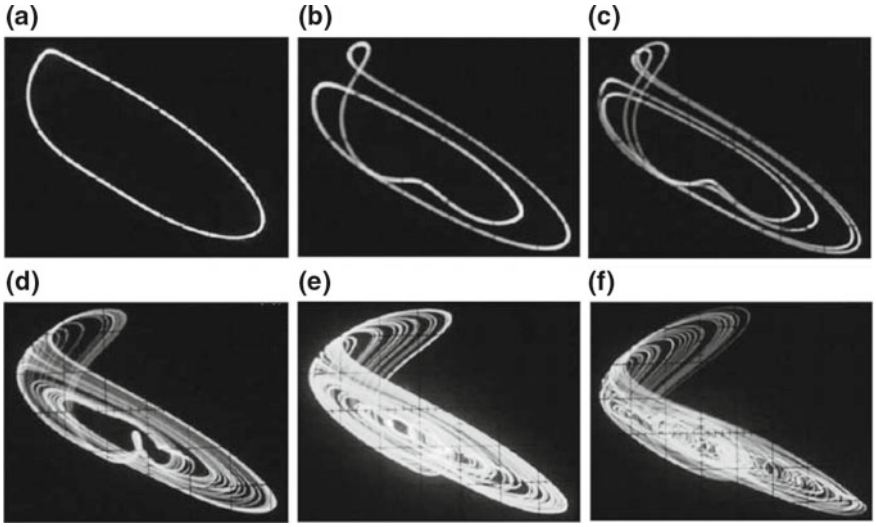

Fig. 2.27 The oscilloscope trace of experimentally obtained phase-plane plots in the $V(t) - V(t - T_D)$ space for variable τ: **a** period-1 at $T_D = 0.15$ ms, **b** period-2 at $T_D = 0.24$ ms, **c** period-4 at $T_D = 0.3$ ms, **d** chaos at $T_D = 0.33$ ms, **e** hyperchaos at $T_D = 0.39$ ms, and **f** hyperchaos at $T_D = 0.44$ ms (for other parameters, see text). V (x-axis): 0.5 v/div; $V(t - T_D)$ (y-axis): 0.5 v/div

change the parameter b. For the delay section, the all-pass filter (APF) is designed with the following parameters: $R \approx 10$ kΩ, $C \approx 10$ nF, and $R_8 = R_9 \approx 2.2$ kΩ. At first, we fix the value of b with $R_7 \approx 17$ kΩ (i.e., $b \approx 1.7$). Now, we vary the delay by varying R. At first, to get a small delay, we use only one APF stage. For $R < 9$ kΩ, the circuit shows a fixed dc value (equilibrium point of the circuit). For $R \geq 9$ kΩ (i.e., $T_D = 0.09$ ms) (approx.), a stable limit cycle appears with a frequency 2380 Hz. Next, we use three blocks of APF; $R \approx 10$ kΩ is taken for the first two blocks (contributing 0.2 ms delay) and vary R of the third block. At $R \approx 3$ kΩ (i.e., $T_D = 0.23$ ms) (approx.), the limit cycle of period-1 loses its stability and a period-2 oscillation emerges. A period-4 behavior is observed at $R \approx 9.5$ kΩ (i.e., $T_D = 0.295$ ms) (approx.). Next, we use four blocks: three blocks have $R \approx 10$ kΩ (contributing a delay of 0.3 ms) and the fourth has $R \approx 1.5$ kΩ (i.e., $T_D = 0.315$ ms), which results in a chaotic oscillation in the circuit. The hyperchaotic attractor is observed beyond $R \approx 7$ kΩ (i.e., $T_D = 0.37$ ms). All the above-mentioned behaviors are shown in Fig. 2.27 (in $V - V(t - T_D)$ space), which depicts the experimental phase-plane plots recorded in an analog oscilloscope.

Next, we set the time delay at $T_D = 0.3$ ms (i.e., $\tau = 3$) by using three APF blocks each having $R \approx 10$ kΩ. To observe the behavior of the system for different b, we vary R_7. For $R_7 \approx 9$ kΩ, the circuit shows a stable limit cycle of frequency 1000 Hz. At $R_7 \approx 16.1$ kΩ, the limit cycle of period-1 loses its stability and a period-2 oscillation emerges. A period-4 behavior is observed at $R_7 \approx 16.71$ kΩ. Chaotic oscillation appears at $R_7 \approx 16.75$ kΩ. Apparently, the circuit enters into

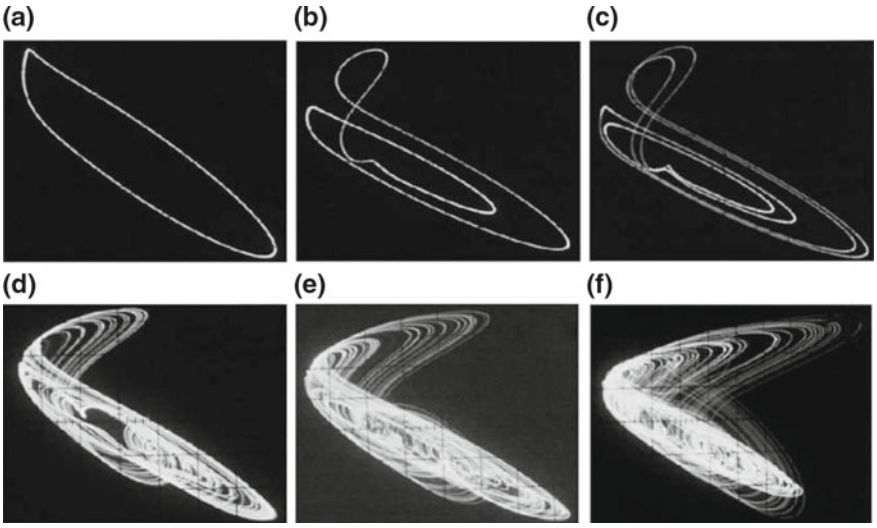

Fig. 2.28 The oscilloscope trace of experimentally obtained phase-plane plots in the $V(t) - V(t - T_D)$ space for variable b: **a** period-1 at $R_7 \approx 12$ kΩ, **b** period-2 at $R_7 \approx 16.4$ kΩ, **c** period-4 at $R_7 \approx 16.72$ kΩ, **d** chaos at $R_7 \approx 16.9$ kΩ, **e** hyperchaos at $R_7 \approx 22.5$ kΩ, and **f** hyperchaos at $R_7 \approx 23.3$ kΩ (for other parameters see text). **a**–**e** V (x-axis): 0.5 v/div; $V(t - T_D)$ (y-axis): 0.5 v/div. **f** V (x-axis): 1 v/div; $V(t - T_D)$ (y-axis): 1 v/div

the hyperchaotic region for $R_7 > 22$ kΩ. With further increase of R_7, the circuit shows a large limit cycle at $R_7 \gtrsim 23.5$ kΩ that indicates the occurrence of boundary crises. All the above-mentioned behaviors (except the large limit cycle) are shown in Fig. 2.28 (in $V - V(t - T_D)$ space), depicting the real-time oscilloscope traces.

2.9 Summary

In this chapter, we have discussed the theory and experiment of two simple first-order time-delayed chaotic systems having single constant delay and two different generic forms of nonlinearities, namely a bimodal and a unimodal nonlinearity. Stability analysis followed by bifurcation analysis established that the systems show a stable limit cycle through a *supercritical Hopf bifurcation*. Detailed numerical simulation proved that with the variation of time delay the systems show a period-doubling route to chaos, hyperchaos, and single scroll or double scroll. Also, if we vary other system parameters keeping the delay constant, the systems show chaotic and hyperchaotic behaviors. The proposed systems have been implemented in analog electronic circuit using off-the-shelf electronic circuit elements. Since a proper choice of system parameters makes the systems hyperchaotic even for a moderate value of time delay, therefore, they can be used as potential hyperchaotic generator for electronic communication applications and chaos-based noise generator systems [5].

http://www.springer.com/978-3-319-70992-5

Time-Delayed Chaotic Dynamical Systems
From Theory to Electronic Experiment
Banerjee, T.; Biswas, D.
2018, XI, 114 p. 71 illus., 19 illus. in color., Softcover
ISBN: 978-3-319-70992-5